Suitability of different Sr_2TaO_3N surface orientations for photocatalytic water oxidation

Maria Bouri and Ulrich Aschauer*

Department of Chemistry and Biochemistry, University of Bern, Bern, Switzerland

E-mail: ulrich.aschauer@dcb.unibe.ch

Abstract

Solar water splitting has attracted much attention as a clean and renewable route to produce hydrogen fuel. Since the oxygen evolution half-reaction (OER) requires high overpotentials, much research has focused on finding catalyst materials that minimize this energy loss. Oxynitrides with a layered perovskite structure have the potential to combine the superior photocatalytic properties of layered perovskite oxides with enhanced visible-light absorption caused by the band gap narrowing due to less electronegative nitrogen ions. In this paper, we study the OER on the (001) and (100) surfaces of the layered oxynitride Sr_2TaO_3N using density functional theory (DFT) calculations to obtain the OER free energy profiles and to determine the required overpotentials at various sites on each surface. We find that the reconstructed grooved (100) surface is most relevant for photocatalysis due to suitable band-edge positions combined with a low overpotential and good carrier mobility perpendicular to the surface.

Introduction

Over recent decades, an ever increasing energy demand together with the negative environmental impact of existing fossil and nuclear energy sources has lead to an intense search for clean and renewable forms of energy and ways to store it. Water splitting to produce hydrogen (H_2) fuel with the energy stored in the H-H chemical bond has attracted much attention in this domain.[1] Fuel cells can convert the produced H_2 back into electricity for various applications with just water as the byproduct. When the energy required for water splitting is provided by solar radiation, the procedure is sustainable and the produced H_2 is environmentally neutral.

The overall water-splitting reaction consists of two half-reactions, the H_2 evolution reaction (HER) being driven by excess electrons and the O_2 evolution reaction (OER) by excess holes. In photocatalysis, recent studies have focused on devices in which a semiconductor photoanode catalyzes the OER and a metal cathode the HER.[2] The excess carriers are generated on the photoanode by cross-gap electron excitation due to incident photons, the excitation providing a potential corresponding to the band gap of the absorbing semiconductor. Ideally an OER photocatalyst will have to provide a potential of 1.23 V but in reality larger potentials are required, the difference being known as the overpotential. Besides interface losses, the overpotential stems from the fact that due to material-dependent adsorbate binding energies the individual reaction steps of the four-step OER have free-energy differences that deviate from the ideal value of 1.23 eV.[3,4] Scaling relations between the different adsorbate adsorption energies lead to minimum theoretical overpotentials of 0.37 V,[5,6] making this half-reaction the bottleneck for water splitting.[7,8] Rendering this technology economically viable crucially requires photoanodes that simultaneously absorb visible light (band gaps below 3 eV) and provide the required overpotential (band gaps above 1.7 eV and adequate band edge positions) while having overpotentials as close as possible to the theoretical minimum.

Perovskite structured oxides with d^0-transition metal B site cations, such as Ti, Nb

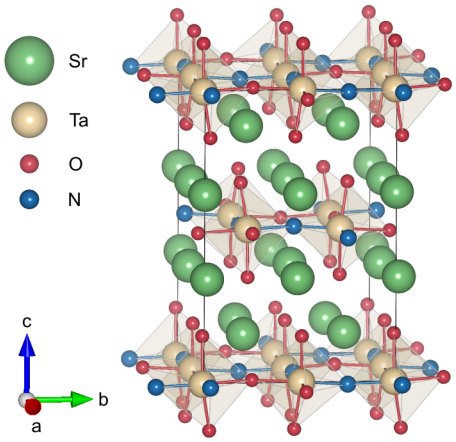

Figure 1: Energetically favoured configuration of the 56-atom bulk Sr_2TaO_3N unit cell with octahedral rotations and the nitrogen atoms adopting a *cis* order on the equatorial sites.

or Ta, were shown to be efficient photocatalysts,[9,10] but their wide band gaps make them inappropriate for visible-light absorption. Substitution of oxygen by less electronegative nitrogen leads to N $2p$ states above the O $2p$ states at the top of the valence band (VB). Since the conduction band (CB) states remain nearly unaffected by this substitution,[11–13] the band gap is reduced and these so-called oxynitrides are suitable for visible-light absorption.

Perovskite materials can occur in multiple layered structure types, among them Ruddlesden-Popper (RP),[14] Dion-Jacobson,[15,16] Aurivillius phases[17] and the Carpy-Galy phases.[18,19] While the layered structures can be exfoliated by proton exchange in acidic medium, they are typically stable in neutral or basic aqueous media.[20–23] Some of these layered structure types were shown to have higher photocatalytic H_2 and O_2 production compared to chemically similar non-layered perovskite oxides.[9] A computational screening of layered perovskite oxides and oxynitrides in the RP structure, including Sr_2TaO_3N, indeed showed that these materials have appropriate band gaps and that their VB and CB edges straddle the water redox levels.[24] Beside these bulk criteria the surface structure as well as the oxidising adsorbates that form under application conditions are expected to affect the OER pathways and the resulting activity of the catalyst. Up to date, computationally studies of the OER mechanism have mostly focused on metal oxide surfaces,[4,6,25] while only few studies investigate

oxynitride surfaces[26,27] and no reports exist for surfaces of layered RP oxynitrides.

Here we use density functional theory (DFT) calculations to determine the thermodynamically most stable terminations under photochemical conditions of the (001) and (100) surfaces of the RP oxynitride Sr_2TaO_3N (bulk structure in Fig. 1), which is one of the few synthesized RP oxynitrides having a d^0-transition metal B site. We then determine the overpotentials of different OER mechanisms via Gibbs free-energy differences of the individual reaction steps on the most relevant terminations. Our findings show that a reconstructed (100) surface is most relevant for photocatalysis due to its stability, a low overpotential when covered with oxygen adsorbates and a valence band maximum that provide sufficient potential to drive the OER. Moreover, the reconstructed RP (100) surface shows better OER activity under operating conditions than the (001) surface of a non-layered material based on the same elements.

Computational Methods

Spin-polarized density functional theory (DFT) calculations were carried out with the Quantum ESPRESSO package[28] using the Perdew-Burke-Ernzerhof (PBE)[29] exchange-correlation functional. We note that more advanced functionals such as hybrids are likely to give more accurate results, in particular for band gaps, but their application would be prohibitively expensive for our large slab calculations. Spin-polarized calculations were found to be important for adsorbate-covered surfaces and result in slightly lower energies, especially when the number of electrons is odd. We note that spin-polarized calculations for clean surfaces yield non-magnetic solutions. Kinetic-energy cut-offs of 35 Ry for the plane wave basis and 280 Ry for the augmented density were used for all calculations. Ultrasoft pseudopotentials[30] with Sr (4s, 4p, 4d, 5s, 5p), Ta (5s, 5p, 5d, 6s, 6p), O (2s, 2p), N (2s, 2p) and H (1s) as valence electrons were used to describe electron-nuclear interactions. Surface geometries were optimised with a force convergence threshold of 0.025 eV/Å. Reciprocal space was sampled

by $4 \times 4 \times 1$ and $4 \times 2 \times 1$ Monkhorst-Pack[31] k-point meshes for the (001) and (100) surfaces respectively that have lateral dimensions of 8.188×8.188 Å and 8.194×12.526 Å.

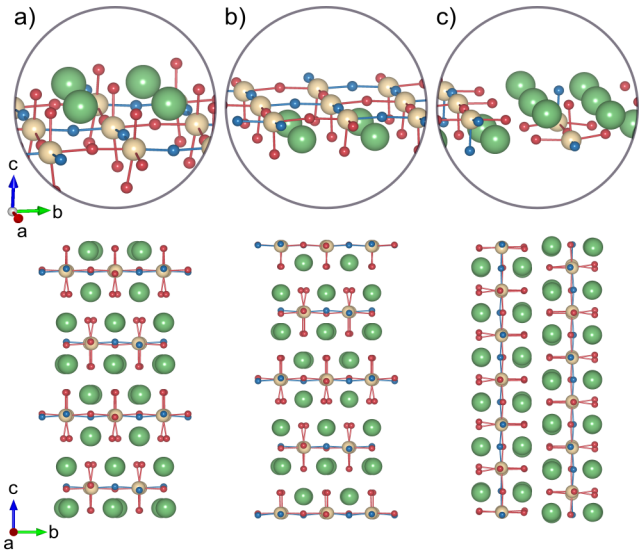

Figure 2: Side and perspective view of a) the SrO-terminated (001), b) the TaON-terminated (001) and c) the (100) surfaces of Sr_2TaO_3N.

Surfaces were constructed by cleaving the fully optimised bulk structure (Fig. 1) with the lowest energy *cis* nitrogen order and octahedral-rotation distortions.[32] Given that surfaces parallel to the {001} planes are usually most stable in the perovskite structure,[33] we consider the (001) and (100) surface orientations, the (001) surface having two different terminations due to the rock-salt layer in the RP structure. The SrO-terminated (001) slab (Fig. 2 a) is constructed by cleaving perpendicular to the [001] direction between two consecutive SrO layers. The resulting slab is symmetric and stoichiometric with 12 atomic layers and a thickness of 22.6 Å. During relaxation the two middle SrO layers are kept fixed. The surface exposes four undercoordinated Sr atoms, surrounded by O atoms, that represent active sites for the OER. The TaON-terminated (001) slab (Fig. 2 b) is created cleaving perpendicular to the [001] direction between a SrO and a TaON layer and adding one extra TaON-layer at the bottom of the slab, resulting in a non-stoichiometric but symmetric 13-layer slab with a thickness of 24.8 Å. The middle three atomic layers are kept fixed during relaxation. The surface exposes four undercoordinated Ta atoms, surrounded by O and N atoms, on which

the OER can take place. The N atoms form a *cis* order in the *ab* plane. The (100) slab (Fig. 2 c) is obtained by cleaving the bulk perpendicular to the [100] direction resulting in a 24.4 Å thick, symmetric and stoichiometric slab with 13 atomic layers. Here, the three middle layers are kept fixed during structural optimization. In this case, the surface exposes four undercoordinated Sr atoms and two undercoordinated Ta atoms that can act as reaction sites for the OER. We note that due to the non-stoichiometric but symmetric slab for the TaON-terminated (001) surface, we cannot directly compare the surface energies of the different slabs. As discussed in our previous work,[32] based on the nature of the broken bonds at the surface, we expect the SrO-terminated (001) surface to have the lowest and the (100) surface to have the highest surface energy. A vacuum of 10 Å is added to all slabs to separate the periodic images along the surface normal direction. A dipole correction[34] was also used along the surface normal direction. Surface Pourbaix diagrams and OER free-energy profiles were computed using the established approach by Nørskov[4,35] (see supporting information section S1). We note that, as discussed in the supporting information, the theoretical overpotential is independent of the pH and for simplicity, we therefore consider pH=0 throughout this work. For surface reconstructions, we also consider formation of ions in alkaline environment (pH=12).

Results and discussion

TaON-terminated (001) surface

Starting from the clean TaON-terminated (001) slab, we investigate the free-energy changes associated with different coverages of hydroxyl and oxygen adsorbates. While for surfaces covered with OH*, we observe the adsorbates to remain nearly upright or to lean slightly towards neighboring N atoms, we find for the fully O*-covered surface a more complex surface adsorbate structure. At high coverage, O* adsorbates tend to tilt significantly to bond with surface N atoms. We consider the situations where all four O* are tilted (4 O* tilt), three

O* are tilted and one remains upright (3 O* tilt) and two of them tilt with two remaining upright (2 O* tilt) as shown in Fig. 3. Somewhat surprisingly, we find that the 3 O* tilt configuration is more stable than the 4 O* tilt structure by 0.93 eV, while the 2 O* tilt configuration is significantly less stable. By comparing the density of states (DOS) of the 3 O* tilt and 4 O* tilt configurations (see supplementary Fig. S4), we see that while the latter has equivalent states associated with all adsorbates, adsorbate states in the former become highly unequal and we see the appearance of an unoccupied N-O state in the band gap just above the Fermi energy. Simultaneously, we see a very marked state associated with the upright O* appearing at lower energies than the states originating from the other O*. This can be interpreted as a charge transfer from π^* antibonding N-O states (see supplementary Fig. S5) to lower lying states associated with the upright O*, resulting in stronger N-O bonds and hence a lower total energy. There is hence a balance between the number of N-O bonds and associated bonding and antibonding states and upright O* states, which is optimal for the 3 O* tilt case.

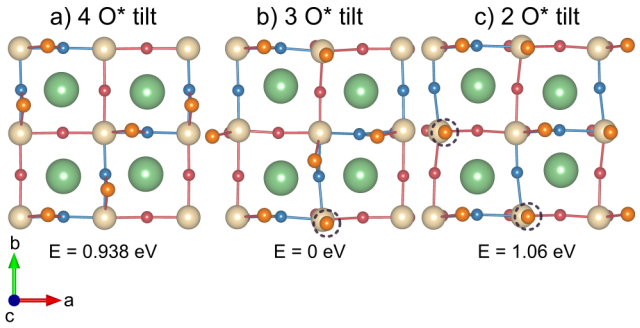

Figure 3: Top views of different configurations of the fully O*-covered TaON-terminated (001) surface: a) four O* atoms tilted towards surface N atoms following the *zig-zag* N-anion order, b) three O* atoms tilted and one O* upright and c) two O* atoms tilted and two O* atoms upright (diagonally aligned). Orange spheres denote adsorbate O* atoms and dotted circles indicate the upright O* atoms.

In Fig. 4 a) we report the energies of surfaces with different adsorbate coverages and configurations with respect to the clean surface as a function of the potential and at pH=0. At potentials close to zero the clean (no adsorbates) surface is most stable, while we observe terminations with a higher coverage of more oxidising adsorbates (O* rather than OH*) to

become increasingly more stable at higher potentials. In particular, our calculations predict that for potentials above 0.25 V the surface is covered with 1/2 monolayer (ML) OH* and 1/2 ML O* where we also observe the O* atoms to tilt and bond with surface N atoms (see supplementary Fig. S2). We note that spurious energy lowering due to charge transfer between adsorbates[36,37] is not expected since all adsorbates are electron acceptors. However, H-bonding between fragments could lead to a more favorable adsorption at high-coverage. For potentials above 1.2 V the surface is covered with 1 ML of O*, assuming the 3 O* tilt structure (Fig. 3 b) discussed above.

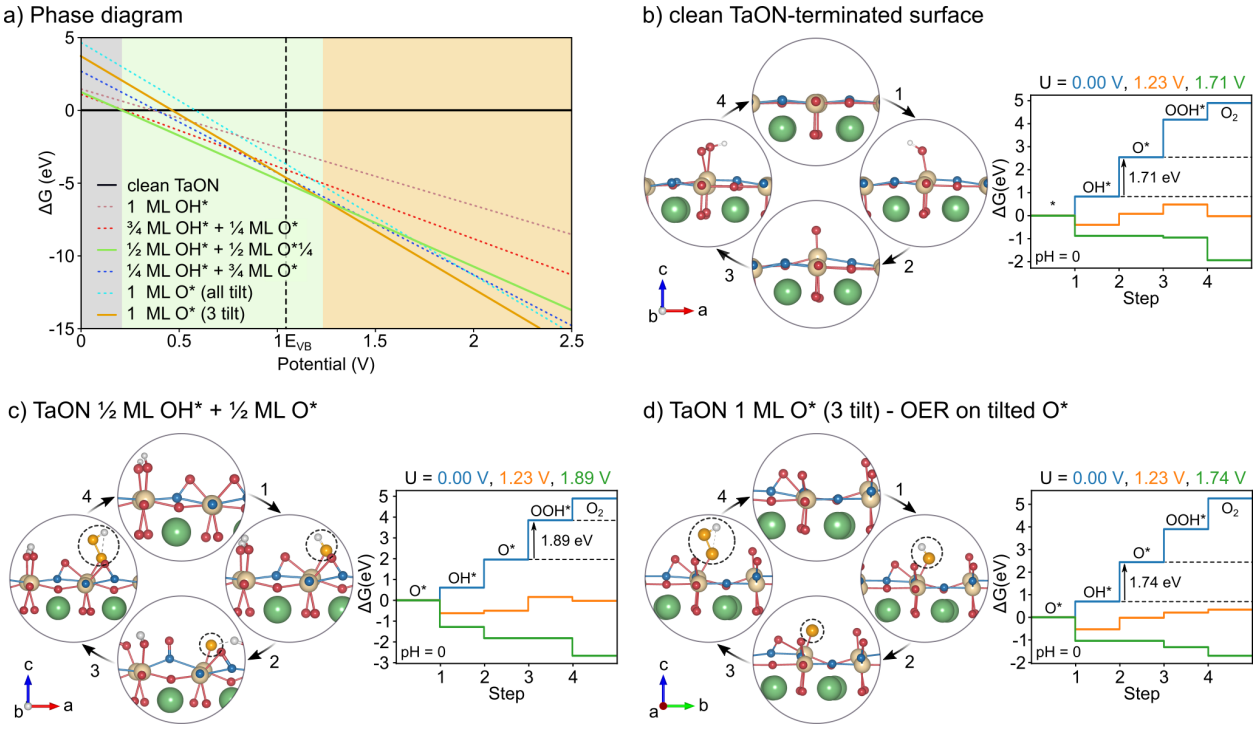

Figure 4: a) Surface Pourbaix diagram of the TaON-terminated (001) surface as well as OER steps (left) and Gibbs free energy diagrams (right) for b) the clean surface, c) the surface covered with 1/2 ML OH* and 1/2 ML O* and d) with 1 ML O* considering the tilted O* as reaction site.

We first investigate the OER on the clean TaON-terminated (001) surface that is relevant at potentials below 0.2 V and calculate the free-energy differences of the four individual proton-coupled-electron transfer (PCET) steps. The surface configurations during the OER are shown in Fig. 4 b. Step 1 corresponds to the deprotonation of one H_2O molecule,

the resulting OH fragment remaining vertically adsorbed on the Ta site and leading to a small outwards relaxation. In step 2, the OH* is further deprotonated to O*, which remains vertically adsorbed on top of the surface Ta atom, while leading to a more marked outward relaxation. The deprotonation of another water molecule in step 3 and the association of the resulting OH fragment with the adsorbed O* leads to the formation of an OOH* on the Ta site which, in step 4 after a final deprotonation, desorbs as an O_2 molecule leaving the surface clean from adsorbates. The free energy diagram (Fig. 4 b) reveals that the overpotential-determining step (ODS) is the formation of O* (step 2). The potential needed for all the OER steps to be downhill is 1.71 V corresponding to a theoretical overpotential of 0.48 V.

Next, we study the OER on the 1/2 ML OH* and 1/2 ML O* covered surface. We consider the OER to happen on one of the tilted O* since the OER on the OH* requires a higher overpotential (see supporting Fig. S3). We find an OOH* intermediate formed on this O* to be unstable and to dissociate into a O* and OH* bound to the same Ta. In other words, it is energetically more favorable to adsorb the OH* resulting from deprotonating the water molecule on the Ta site rather than to form the OOH*. We hence proceed with a different mechanism, in which the initial tilted O* remains passive and the OER proceeds by the conventional mechanism as if the Ta site was bare (step 1 being the adsorption of the OH* on the Ta site), resulting in an over-coordinated Ta site (Fig. 4 c). The free energy diagram reveals that the ODS is the formation of the OOH* with a free energy difference of 1.89 eV. This free energy change corresponds to an overpotential of 0.66 V, slightly larger than on the clean surface. A recombination mechanism of the second O* with the tilted O* is highly unfavorable in all situations (see supporting information Section S2).

Finally, we consider the OER on the energetically most stable fully O*-covered 3 O* tilt surface (Fig. 3 b). As discussed above, the states associated with the tilted and upright O* are located at very different energies and we thus consider these sites independently for the OER. Just as for the 1/2 ML O* and 1/2 ML OH* covered surface, we find that the OOH*

intermediate formed on a tilted O* is unstable and dissociates into a O* and OH* bound to the same Ta and therefore proceed with the mechanism described above. The free energy diagram (Fig. 4 d) reveals that the limiting step in this case is the deprotonation of OH* (step 2). The potential required for the process to become thermodynamically favourable is 1.74 V, which represents an overpotential of 0.51 V. For the OER on the upright O* (supporting Fig. S7) we find the OOH* intermediate to be stable and calculate the Gibbs free energy change for the conventional mechanism. The ODS is the formation of the OOH* intermediate with a free energy change of 2.51 eV corresponding to an overpotential of 1.28 V, which is much higher than the one obtained on the tilted O*.

SrO-terminated (001) surface

Fig. 5 a) shows the free energy relative to the clean surface for different adsorbate coverages of the SrO-terminated (001) surface as a function of the applied potential. For potentials lower than 0.70 V, the clean surface (with no adsorbates) is most stable, whereas for potentials in the range 0.70-1.0 V the surface covered with 3/4 ML OH* is the most stable and in the range 1.0-1.16 V the surface fully covered with OH* is the most stable, while the SrO surface covered with 1/2 ML of OH* and 1/2 ML of O* atoms becomes stable in a small range of 1.16-1.44 V. For even higher potentials the fully O*-covered surface is thermodynamically favoured.

We first investigate the OER on the clean surface (Fig. 5 b). The OER proceeds by the conventional mechanism, with adsorbates in a bridge site between two Sr atoms, which is in agreement with other studies of O* adsorption on the A cations of perovskite oxide (001) surfaces.[38,39] We note that the binding of the O* adsorbate results in a significant shift of the purely ionic and hence weakly bound surface Sr atoms while the OOH* and OH* adsorbates do not lead to such a change in surface structure. This displacement of the surface atoms by the adsorbate is indicative of a low stability of the SrO-terminated surface in an oxidising environment and implies that this surface termination may not be very relevant for the OER.

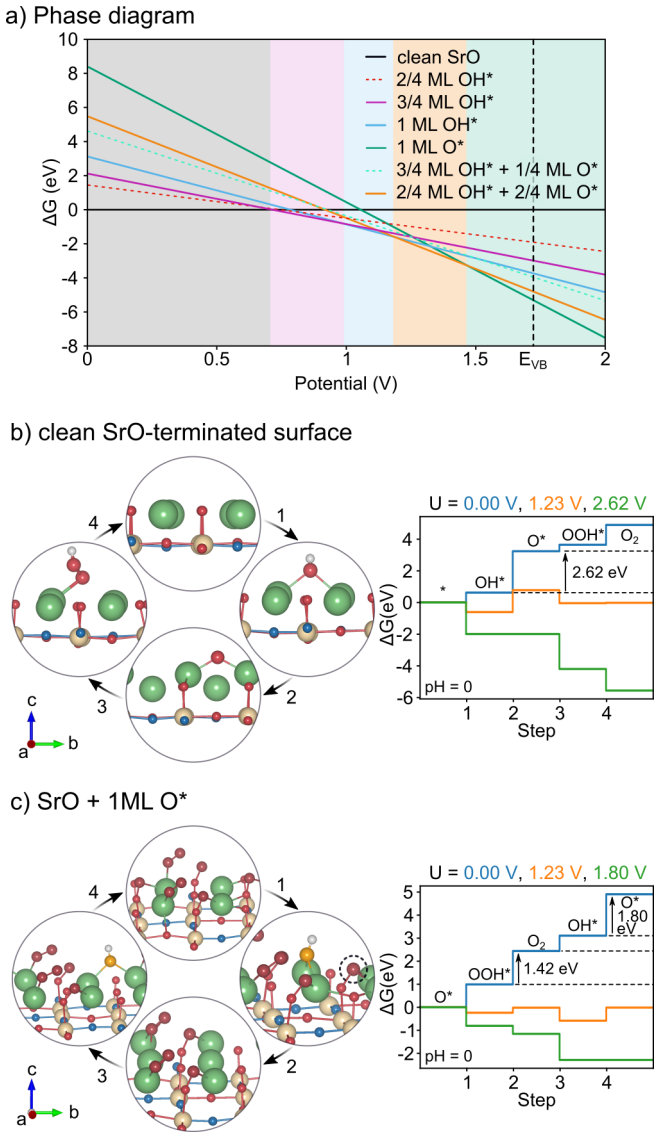

Figure 5: a) Surface Pourbaix diagram of the SrO-terminated surface as well as OER steps (left) and Gibbs free energy diagrams (right) for b) the clean and c) the fully O* covered surface.

The free energy profile based on these potentially unstable structures (Fig. 5 b) shows that the ODS corresponds to the formation of O* and has a free energy difference of 2.62 eV, corresponding to a theoretical overpotential of 1.39 V. This overpotential is significantly higher than on the TaON termination, which can be related to the too weak ionic binding of the O* on the SrO termination in contrast with the stronger covalent Ta-O bond. Indeed we find the O* binding energy on the SrO termination to be 0.73 eV more positive (weaker bond) than on the TaON surface (see Table 1 at the end of the article).

Next, we study the OER on the fully O*-covered surface (Fig. 5 c) which is the most stable termination at application-relevant potentials > 1.23 V. In this configuration, two O* atoms recombine and form an O_2 molecule adsorbed on a Sr atom with the remaining two O* forming bonds with the surface O atoms. We note that this O_2 formation leads to a spurious energy lowering. We consider the OER on the still adsorbed O*. The mechanism that we find to be most favourable, does not involve OOH*, but proceeds by formation of OH* species in bridge positions between Sr sites and after deprotonation of OH* to O* their coupling with a pre-adsorbed O* (circled in Fig. 5 c) and desorption of O_2, with a small energy difference of 1.45 eV. This mechanism has as the ODS the deprotonation of OH* with a free energy difference of 1.80 eV, corresponding to an overpotential of 0.57 V. The overpotential under these conditions is lower than on the clean SrO surface and comparable to the ones obtained for the TaON-terminated surface.

(100) surface

We further study the (100) surface of Sr_2TaO_3N, which exposes Sr and Ta reaction sites at a ratio of 4:2. We investigate different O* and OH* coverages on both sites (Fig. 6 a) in order to determine the preferred coverage of the surface as a function of the potential. We see that the OH* covered Ta sites (1/3 ML) become more stable for potentials between 0.15 V and 0.22 V while for higher potentials up to 0.9 V the surface 2/3 ML covered with a combination of O* and OH* surface is most stable. The fully O*-covered surface is most

stable for potentials higher than 0.9 V. On the resulting fully O*-covered surface, we however notice an unstable surface structure with large displacements of Sr atoms and desorption of O_2 and ON (supplementary Fig. S9). We thus assume that this fully O*-covered (100) surface will reconstruct as discussed in the next section.

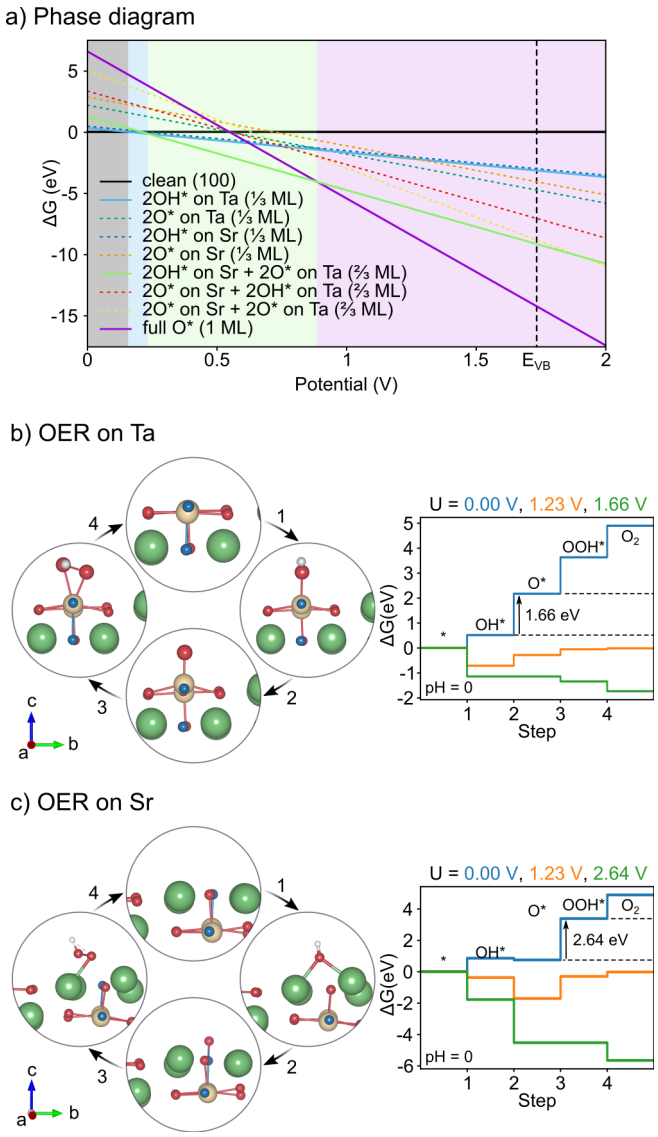

Figure 6: a) Surface Pourbaix diagram of the (100) surface (top) as well as OER steps (left) and the Gibbs free energy diagrams (right) for b) the Ta and c) the Sr site on the clean (100) surface.

We investigate the OER on the clean (100) surface, treating the two reaction sites separately (Fig. 6 b and c). Interestingly, we observe that despite the ODS being the same

(step 2) on the Sr and Ta terminated clean (001) surfaces as determined above, on the (100) surface the ODS changes to step 3 for the Sr site. The overpotential on the Ta site (0.43 V) is significantly lower than on the Sr site (1.41 V), which agrees with the higher activity of the Ta site compared to the Sr site already found above for the (001) surface terminations. Still, the (100) surface requires higher overpotentials than the (001) surfaces, implying a lower OER reactivity.

Reconstructed grooved (100) surface

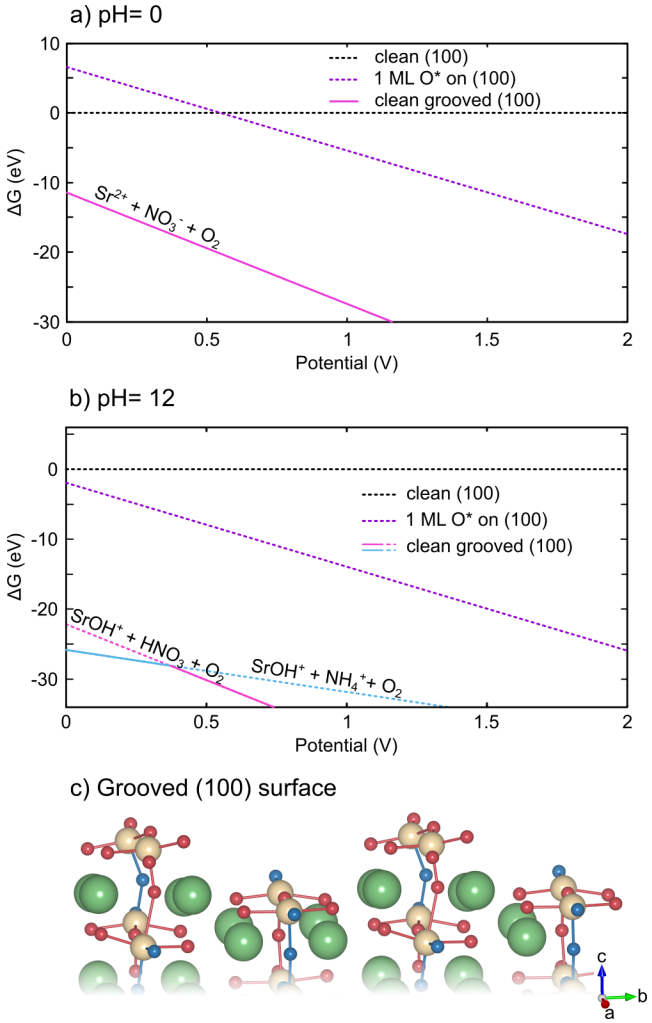

Figure 7: Stability of the O*-covered flat and grooved (100) surfaces with respect to the clean (100) surface at a) pH=0 and b) pH=12. The structure of the grooved (100) surface is shown in the insets.

As mentioned above, for potentials above 0.8 V, the fully O*-covered surface is the most stable but our calculations show an instability of the surface. We hence investigate the OER on a surface where the unstable Sr sites as well as their coordinating O and N atoms have been removed (see supporting information Section S4), resulting in a groove, while surface N atoms are substituted by O atoms to cancel polarity. The first alteration is motivated by the known instability of surface Sr species,[38,39] while the second is analogous to filling of surface N vacancies by O adsorbates under OER conditions[40] and leads to a large gain in electrostatic energy.[41] The new surface shown in the inset of Fig. 7, exposes two Ta atoms on the upper terrace as reactive sites surrounded by O atoms and two Ta on the lower terrace surrounded by both N and O atoms.

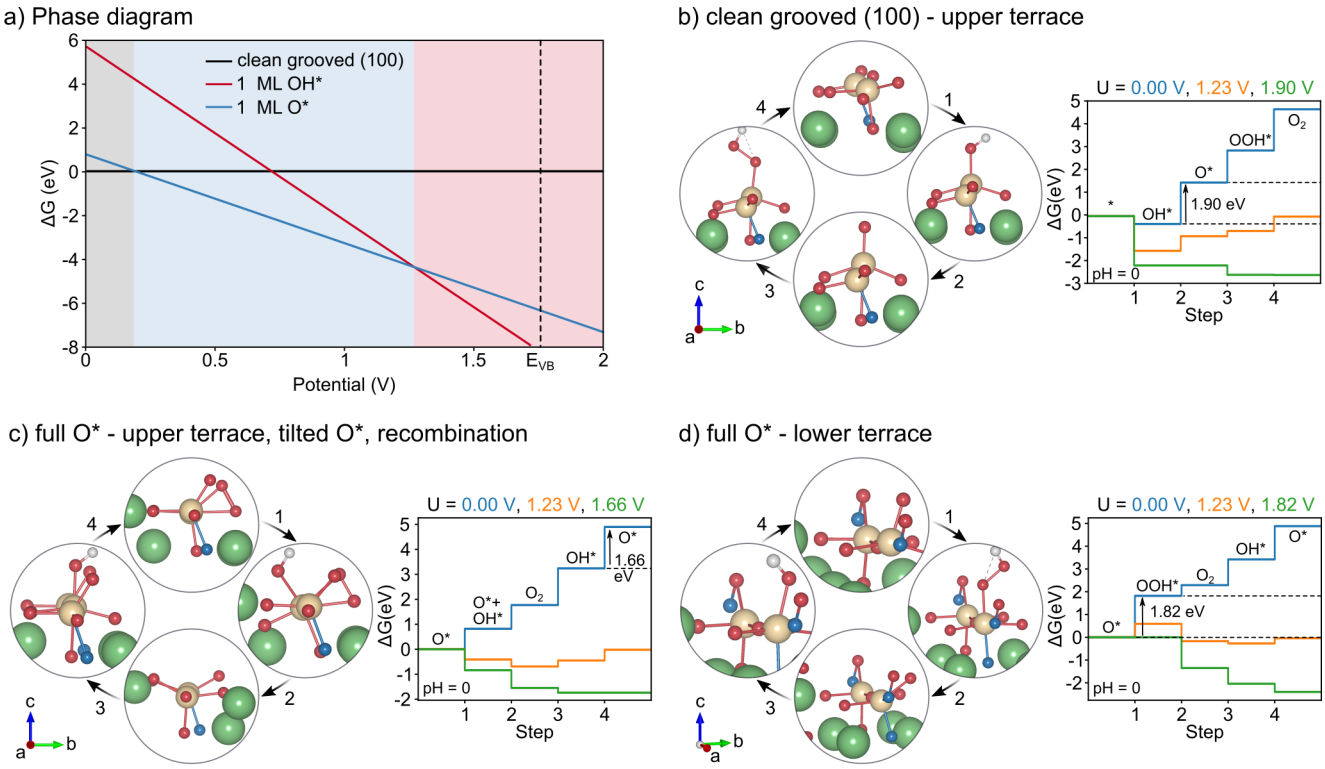

Figure 8: a) Surface Pourbaix diagram of the grooved (100) surface as well as OER steps (left) and Gibbs free energy diagram (right) for b) the clean and c)-d) different sites on the 1 ML-O*-covered surface.

We investigate the stability of the grooved surface with respect to the clean, non-reconstructed (100) surface (Fig. 7), considering that the removed Sr, N, and O atoms form solvated ions

in water. Following the thermodynamic approach proposed in other works,[35,42] we calculate the free energy of the reconstructed (100) surface considering both the formation energy of the surface vacancies on the clean (100) surface and the formation energy of the solvated ions in both acidic (pH=0) and alkaline environment (pH=12) (see supporting information section S1). Interestingly, we find that the reconstructed grooved surface is favoured over both the flat, clean and O*-covered surfaces at all potentials and under both acidic and alkaline conditions, showing the preference of the (100) surface to reconstruct in contact with water. We note that this point-defect based surface restructuring could miss a complete surface restructuring, such as the formation of a different phase at the surface under OER conditions, however a more complete sampling using only computation is prohibitive at this stage.

We first investigate the OER on the Ta-sites of both the upper and lower terrace of the grooved (100) surface without adsorbates (supporting Fig. S11) considering the conventional mechanism (results for other sites can be found in the supporting information). We find that the Ta-site of the upper terrace (bonded with a O atom along the z direction) requires the lowest overpotential (Fig. 8 b) having as ODS the formation of the O* with a free energy difference of 1.90 eV corresponding to an overpotential of 0.67 V, higher than the one obtained on the clean TaON-terminated surface.

Next, we investigate the OER on the O*-covered termination, which we find to be more stable than the clean grooved surface for potentials higher than 1.26 V (Fig. 8 a). The two O* atoms on the upper terrace are adsorbed in a tilted configuration on the Ta atoms with one O* bonding with a surface O while the other does not form such a bond and we consider the OER on the two sites separately. We find the formation of OOH* to be unstable when O* is bonded with the surface O atom and hence consider the conventional mechanism on the over-coordinated Ta site similarly to the O*-covered TaON-terminated (001) surface (supporting Fig. S13), for which we find an overpotential of 0.99 V. Interestingly, when considering an alternative mechanism involving the recombination of the O* and the deprotonated OH*

intermediates and their desorption as an O_2 molecule, we find a lower overpotential (Fig. 8 c). The ODS for this mechanism is the formation of the O* intermediate on the empty Ta site with a free energy difference of 1.66 eV, corresponding to an overpotential of 0.55 V. We want to note that this recombination may however be associated with a kinetic barrier. On the O* that does not bind with surface O, we find the ODS to be the oxidation of OH* with a free energy change of 2.21 eV corresponding to an overpotential of 0.98 V (supporting Fig. S14), which is larger than on the bonded O*, in agreement with the above results for the 1 ML O* covered TaON-terminated (001) surface.

We further investigate the OER on the lower terrace, which exposes one upright O* and one O* tilted and bonded with a surface N atom (Fig. 8 d). Interestingly, we find that the conventional mechanism on the upright O* results in a low overpotential of 0.59 V in contrast to the other upright cases. Here step 1 (OOH* formation) is the ODS similarly to the case of the upright O* on the TaON-terminated surface. We can relate this to large structural relaxation (by 0.24 Å) of the Ta atom along the c direction, which results in the largest energy changes during step 1. We note that the recombination mechanism on the lower Ta-site has a significantly higher overpotential.

Positions of the valence-band maxima

It is essential to determine the position of the valence-band edge relative to the normal hydrogen electrode (NHE) since this energy difference represents the OER bias potential resulting from the photo-excitation of electrons. We use an empirical method to estimate the band edges of bulk Sr_2TaO_3N, which is based on the electronegativities of the contituent elements, $\chi_{element}$, and the bandgap, E_{gap} of the bulk.[24] The band edges for the RP oxynitride Sr_2TaO_3N within this approximation are:

$$E_{VB,CB} = E_0 + (\chi_{Sr}^2 \chi_{Ta} \chi_O^3 \chi_N)^{1/7} \pm E_{gap}/2 \quad (1)$$

where E_0 is the difference between the vacuum level and the NHE (-4.5 eV). This empirical formula allows us to use the more accurate E_{gap} of bulk Sr_2TaO_3N (2.005 eV) determined using the hybrid functional HSE06.[32] Using this value and the electronegativities calculated from the electron affinities and the ionization potentials as proposed by Mulliken,[43] we find the VB and CB edges at 1.73 eV and -0.28 eV *vs* NHE respectively. The VB edge that we are mostly interested in for water oxidation, is in agreement with the one previously determined based on G_0W_0 calculation of E_{gap} and the same empirical method.[24]

To further estimate the band edges of the various surfaces, we align the PBE density of states (DOS) of bulk Sr_2TaO_3N and its (001) and (100) surfaces at a Sr 4*s* semi-core state (Fig. 9). Compared to directly extracting band edges from our PBE slab calculations, this approach has the advantage of determining them relative to a more accurate HSE06-based bulk band edge. We observe that the valence-band maximum (VBM) of both the SrO-terminated (001) surface (0.01 eV lower) and the (100) surface (0.025 eV lower) are in the same range as the one of the bulk while the VBM of the reconstructed (100) surface is 0.06 eV lower in energy. The VBM of the TaON-terminated (001) surface however is located at a significantly higher energy (0.665 eV) compared to all other VBMs due to the surface nitrogen states that are destabilised with respect to the bulk states.[32]

Since direct hybrid functional calculations of surface band edges are prohibitively expensive, we here consider the above values relative to the bulk hybrid functional VBM (1.73 eV) to estimate surface VBMs with respect to the NHE, which are 1.73 eV, 1.06 eV, 1.75 eV, and 1.78 eV for the SrO-terminated (001), the TaON-terminated (001), the (100) surface and the grooved (100) surface respectively. These VBM positions correspond to the potential vs. NHE that light irradiation provides and will determine the adsorbate coverage of the surface under illumination. We note that for all surfaces a full O* coverage is preferred at these potentials as indicated by the vertical E_{VB} line in the various surface Pourbaix diagrams. The difference between the respective VBM and the water oxidation potential (1.23 V vs. NHE) corresponds to the overpotential the surface provides. The TaON-terminated (001) surface

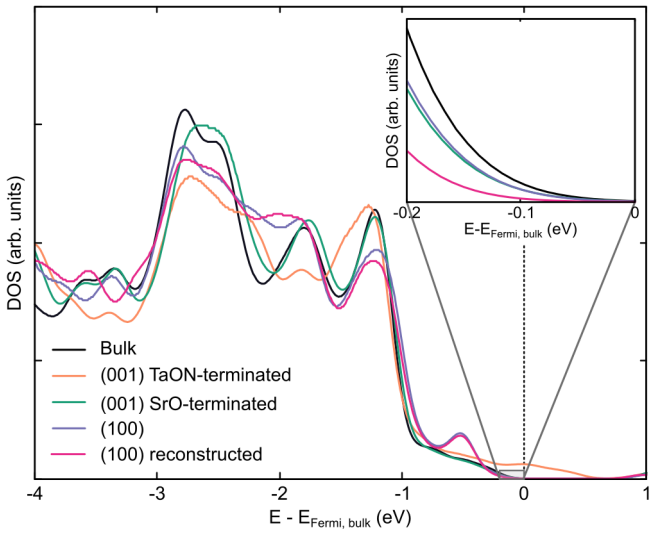

Figure 9: Electronic density of states (DOS) of bulk Sr_2TaO_3N and its surfaces, obtained using PBE. The DOS have been aligned at a Sr 4*s* semi-core state -18.6 eV below the Fermi energy and each DOS is scaled according to the number of electrons in the respective structure.

does not provide a positive overpotential and is, despite it's promising catalytic activity, not able to drive the OER without an external potential. For the SrO-terminated (001) surface, the provided overpotential of 0.5 V is slightly smaller than the smallest computed OER overpotential of 0.56 V for the O*-covered surface, rendering this termination also unable to drive the OER. The (100) surface in its stable reconstructed form provides an overpotential of 0.55 V, which is larger than the smallest computed OER overpotential (0.47 V) and the reconstructed (100) surface can thus drive the OER.

Comparison of OER on (001) surfaces with layered and non-layered structure

Experimental studies have compared the photocatalytic activity of layered with non-layered perovskite-oxides and have shown the higher photocatalytic activity of the layered materials.[9,44,45] In this section, we thus compare the overpotentials obtained for the (001) surfaces of layered Sr_2TaO_3N with the ones previously reported for non-layered $SrTaO_2N$ (001) surfaces.[27] In that work, spin-restricted calculations were performed and a O*-covered surface

with 4 O* tilted was considered but we find, in analogy to the above results, that a termination with 3 tilted and one upright O* is more favorable also for $SrTaO_2N$. In Table 1 we thus report, in addition to this 4 O* tilt case, the overpotential also for the energetically preferred 3 O* tilt structure obtained by spin-polarised calculations.

Table 1: Comparison of OER overpotentials, ODS and O binding energies of surfaces with layered and non-layered structure. For the 3 O* tilt structure, the results in parentheses correspond to the upright O* site.

	Overpotential		ODS		O Binding Energy	
Surface termination	layered	non-layered	layered	non-layered	layered	non-layered
(001) SrO (clean)	1.39	1.14[27]	2	2[27]	3.22	2.21
(001) SrO (1 ML-O*)	0.57	1.14[27]	4	2[27]	2.24	2.03
(001) TaON (clean)	0.48	1.01[27]	2	3[27]	2.50	0.62
(001) TaON (1 ML-O*, 4 O* tilted)	0.45	0.88[27]	3	3[27]	1.57	0.85
(001) TaON (1 ML-O*, 3 O* tilted)	0.51(1.28)	0.67(1.31)	2(1)	3(1)	2.28	1.38

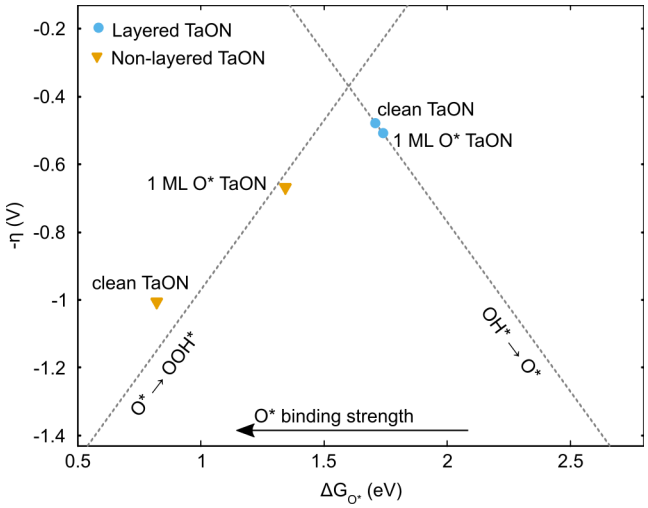

Figure 10: Volcano plot of the free energy difference of step 2 (ΔG_{O^*}) and the OER overpotential (η) for both layered and non-layered TaON-terminated (001) surfaces.

For the clean SrO-terminated (001) surface we predict a larger overpotential on the layered compared to the non-layered material even though the ODS is the same. Since the O* binding energy on the non-layered surface is 1.01 eV lower (stronger) than on the layered surface, the oxidation of OH* to O* requires less energy according to the universal scaling relations.[5,6] For the O*-covered SrO-terminated (001) surface, we find a different mechanism

to be favored on the layered and the non-layered surface, which is reflected in the very different overpotentials, the layered material being significantly more active.

For the clean TaON-terminated (001) surface on the other hand we predict a significantly smaller OER overpotential for the layered surface compared to the non-layered one, the ODS being step 3 (OOH* formation) and step 2 (O* formation) respectively. This is due to the much stronger binding of O* to the non-layered surface, which, according to the commonly-used volcano analysis as a function of the free energy of step 2,[3,6,46] indicates that the two materials are located on different sides of the volcano tip. While the layered material is located on the right branch and limited by weak O* adsorption, the non-layered material is located on the left branch and limited by strong O* adsorption as shown in Fig. 10. We find that a full ML O* adsorbate coverage slightly increases the overpotential of the layered material, while it decreases the overpotential of the non-layered material. We can relate this to the fact that increasing the O* coverage decreases the binding strength of individual O* adsorbates. Given that the non-layered material is located on the left branch of the activity volcano, this change will shift the overpotential towards the tip of the volcano (Fig. 10). The layered material, already being on the right branch, moves further away from the tip, resulting in a higher overpotential. Despite this small increase in overpotential, the layered material still requires a lower overpotential than the non-layered material rendering it more OER active. For the fully O*-covered TaON-terminated (100) surface the trend of a higher activity of the layered material persists when considering the energetically less favorable 4 O* tilted surface structure. However, we see that the ODS changes, the stronger O* binding in the 4 O* tilted structure shifting the surface to the left branch of the volcano.

Conclusions

We investigated the surface adsorbate coverage and the OER mechanisms on the (001) and (100) surfaces of Sr_2TaO_3N. For all surfaces, we predict full coverage with O* adsorbates

under light irradiation. We observe complex surface structures at high O* coverages with O* forming bonds with surface N atoms. The potential provided by the valence-band edge of the TaON-terminated (001) surface is more negative than the lowest OER potential and hence not sufficient to drive the reaction. The same is true for the SrO-terminated (001) surface, which is hence also unable to drive the OER. For the (100) surface on the other hand, we predict a grooved reconstruction to be most stable that has a low overpotential of 0.47 V and provides a sufficient potential to drive the OER. Combined with the high carrier mobility perpendicular to the surface,[32] this renders the (100) surface the most relevant Sr_2TaO_3N surface to photocatalyze the OER. Comparing the reconstructed grooved (100) surface of the layered Sr_2TaO_3N with the TaON-terminated (001) surface of non-layered $SrTaO_2N$, we find the smallest overpotential for the Ta site on the lower terrace of the former, which is in agreement with the improved catalytic activity of layered perovskite materials.

Acknowledgement

This research was funded by the SNF Professorship Grant PP00P2_157615. Calculations were performed on UBELIX (http://www.id.unibe.ch/hpc), the HPC cluster at the University of Bern as well as SuperMUC at GCS@LRZ, Germany, for which we acknowledge PRACE for awarding us access.

Supporting Information Available

Supporting Information. Additional method details and results for additional surfaces and mechanisms. This material is available free of charge via the internet at http://pubs.acs.org.

References

(1) Turner, J. A. Sustainable hydrogen production. *Science* **2004**, *305*, 972–974.

(2) Grätzel, M. Photoelectrochemical cells. *Nature* **2001**, *414*, 338–344.

(3) Rossmeisl, J.; Logadottir, A.; Nørskov, J. K. Electrolysis of water on (oxidized) metal surfaces. *Chemical Physics* **2005**, *319*, 178–184.

(4) Valdés, Á.; Qu, Z. W.; Kroes, G. J.; Rossmeisl, J.; Nørskov, J. K. Oxidation and photo-oxidation of water on TiO_2 surface. *Journal of Physical Chemistry C* **2008**, *112*, 9872–9879.

(5) Koper, M. T. Theory of multiple proton–electron transfer reactions and its implications for electrocatalysis. *Chemical Science* **2013**, *4*, 2710–2723.

(6) Man, I. C.; Su, H.-Y.; Calle-Vallejo, F.; Hansen, H. A.; Martínez, J. I.; Inoglu, N. G.; Kitchin, J.; Jaramillo, T. F.; Nørskov, J. K.; Rossmeisl, J. Universality in oxygen evolution electrocatalysis on oxide surfaces. *ChemCatChem* **2011**, *3*, 1159–1165.

(7) Greeley, J.; Markovic, N. M. The road from animal electricity to green energy: Combining experiment and theory in electrocatalysis. *Energy & Environmental Science* **2012**, *5*, 9246–9256.

(8) Peter, L. M.; Doyle, R. L.; Lyons, M. E. In *Photoelectrochemical solar fuel production*; Giménez, S., Bisquert, J., Eds.; Springer International Publishing, 2016.

(9) Kudo, A.; Miseki, Y. Heterogeneous photocatalyst materials for water splitting. *Chemical Society Reviews* **2009**, *38*, 253–278.

(10) Takata, T.; Pan, C.; Domen, K. Recent progress in oxynitride photocatalysts for visible-light-driven water splitting. *Science and Technology of Advanced Materials* **2015**, *16*, 033506.

(11) Fuertes, A. Metal oxynitrides as emerging materials with photocatalytic and electronic properties. *Materials Horizons* **2015**, *2*, 453–461.

(12) Porter, S. H.; Huang, Z.; Woodward, P. M. Study of anion order/disorder in $RTaN_2O$ (R = La, Ce, Pr) perovskite nitride oxides. *Crystal Growth and Design* **2014**, *14*, 117–125.

(13) Ji, S. M.; Borse, P. H.; Kim, H. G.; Hwang, D. W.; Jang, J. S.; Bae, S. W.; Lee, J. S. Photocatalytic hydrogen production from water–methanol mixtures using N-doped $Sr_2Nb_2O_7$ under visible light irradiation: effects of catalyst structure. *Physical Chemistry Chemical Physics* **2005**, *7*, 1315–1321.

(14) Ruddlesden, S. N.; Popper, P. New compounds of the K_2NiF_4 type. *Acta Crystallographica* **1957**, *10*, 538–539.

(15) Dion, M.; Ganne, M.; Tournoux, M. Nouvelles familles de phases $M^IM^{II}{}_2Nb_3O_{10}$ a feuillets "perovskites". *Materials Research Bulletin* **1981**, *16*, 1429–1435.

(16) Jacobson, A.; Johnson, J. W.; Lewandowski, J. Interlayer chemistry between thick transition-metal oxide layers: synthesis and intercalation reactions of $K[Ca_2Na_{n-3}Nb_nO_{3n+1}]$ ($3 \leq n \leq 7$). *Inorganic Chemistry* **1985**, *24*, 3727–3729.

(17) Aurivillius, B. The structure of Bi_2NbO_5F and isomorphous compounds. *Arkiv for Kemi* **1953**, *5*, 39–47.

(18) Lichtenberg, F.; Herrnberger, A.; Wiedenmann, K. Synthesis, structural, magnetic and transport properties of layered perovskite-related titanates, niobates and tantalates of the type $A_nB_nO_{3n+2}$, $A'A_{k-1}B_kO_{3k+1}$ and $A_mB_{m-1}O_{3m}$. *Progress in Solid State Chemistry* **2008**, *36*, 253–387.

(19) Valdez, M. N.; Spaldin, N. A. Origin and evolution of ferroelectricity in the layered rare-earth-titanate, $R_2Ti_2O_7$, Carpy-Galy phases. *Polyhedron* **2019**, *171*, 181 – 192.

(20) Schaak, R. E.; Mallouk, T. E. Prying apart Ruddlesden-Popper phases: Exfoliation into sheets and nanotubes for assembly of perovskite thin films. *Chemistry of Materials* **2000**, *12*, 3427–3434.

(21) Ida, S.; Okamoto, Y.; Matsuka, M.; Hagiwara, H.; Ishihara, T. Preparation of Tantalum-Based Oxynitride Nanosheets by Exfoliation of a Layered Oxynitride, $CsCa_2Ta_3O_{10x}N_y$, and Their Photocatalytic Activity. *Journal of the American Chemical Society* **2012**, *134*, 15773–15782.

(22) da Silva Maia, A.; Cheviré, F.; Demange, V.; Bouquet, V.; Pasturel, M.; Députier, S.; Lebullenger, R.; Guilloux-Viry, M.; Tessier, F. Preparation of niobium based oxynitride nanosheets by exfoliation of Ruddlesden-Popper phase precursor. *Solid State Sciences* **2016**, *54*, 17 – 21.

(23) Lee, W.-J.; Jung, H.; Kim, Y.-I.; Paek, S.-M. Synthesis and X-ray absorption spectroscopic analysis of exfoliated perovskite oxynitride nanosheets obtained from $LiLaTa_2O_{6.15}N_{0.57}$ precursor. *Journal of Solid State Chemistry* **2019**, *269*, 285 – 290.

(24) Castelli, I. E.; García-Lastra, J. M.; Hüser, F.; Thygesen, K. S.; Jacobsen, K. W. Stability and bandgaps of layered perovskites for one- and two-photon water splitting. *New Journal of Physics* **2013**, *15*, 105026.

(25) Bajdich, M.; García-Mota, M.; Vojvodic, A.; Nørskov, J. K.; Bell, A. T. Theoretical investigation of the activity of cobalt oxides for the electrochemical oxidation of water. *Journal of the American Chemical Society* **2013**, *135*, 13521–13530.

(26) Montoya, J. H.; Garcia-Mota, M.; Nørskov, J. K.; Vojvodic, A. Theoretical evaluation of the surface electrochemistry of perovskites with promising photon absorption properties for solar water splitting. *Physical Chemistry Chemical Physics* **2015**, *17*, 2634–2640.

(27) Ouhbi, H.; Aschauer, U. Water oxidation chemistry of oxynitrides and oxides: Comparing $NaTaO_3$ and $SrTaO_2N$. *Surface Science* **2018**, *677*, 258–263.

(28) Giannozzi, P. et al. QUANTUM ESPRESSO: A modular and open-source software project for quantum simulations of materials. *Journal of Physics: Condensed Matter* **2009**, *21*, 395502.

(29) Perdew, J. P.; Burke, K.; Ernzerhof, M. Generalized gradient approximation made simple. *Physical Review Letters* **1996**, *77*, 3865–3868.

(30) Vanderbilt, D. Soft self-consistent pseudopotentials in a generalized eigenvalue formalism. *Physical Review B* **1990**, *41*, 7892–7895.

(31) Monkhorst, H. J.; Pack, J. D. Special points for Brillouin-zone integrations. *Physical Review B* **1976**, *13*, 5188–5192.

(32) Bouri, M.; Aschauer, U. Bulk and surface properties of the Ruddlesden–Popper oxynitride Sr_2TaO_3N. *Physical Chemistry Chemical Physics* **2018**, *20*, 2771–2776.

(33) Eglitis, R.; Popov, A. Systematic trends in (001) surface ab initio calculations of ABO_3 perovskites. *Journal of Saudi Chemical Society* **2018**, *22*, 459 – 468.

(34) Bengtsson, L. Dipole correction for surface supercell calculations. *Physical Review B* **1999**, *59*, 12301.

(35) Hansen, H. A.; Rossmeisl, J.; Nørskov, J. K. Surface Pourbaix diagrams and oxygen reduction activity of Pt, Ag and Ni (111) surfaces studied by DFT. *Physical Chemistry Chemical Physics* **2008**, *10*, 3722–3730.

(36) Castelli, I. E.; Man, I.-C.; Soriga, S.-G.; Parvulescu, V.; Halck, N. B.; Rossmeisl, J. Role of the band gap for the interaction energy of coadsorbed fragments. *The Journal of Physical Chemistry C* **2017**, *121*, 18608–18614.

(37) Castelli, I. E.; Soriga, S. G.; Man, I. C. Effects of the cooperative interaction on the diffusion of hydrogen on MgO (100). *The Journal of chemical physics* **2018**, *149*, 034704.

(38) Akbay, T.; Staykov, A.; Druce, J.; Téllez, H.; Ishihara, T.; Kilner, J. A. The interaction of molecular oxygen on LaO terminated surfaces of La_2NiO_4. *Journal of Materials Chemistry A* **2016**, *4*, 13113–13124.

(39) Halwidl, D.; Stöger, B.; Mayr-Schmölzer, W.; Pavelec, J.; Fobes, D.; Peng, J.; Mao, Z.; Parkinson, G. S.; Schmid, M.; Mittendorfer, F.; Redinger, J.; Diebold, U. Adsorption of water at the SrO surface of ruthenates. *Nature Materials* **2016**, *15*, 450–455.

(40) Ouhbi, H.; Aschauer, U. Nitrogen loss and oxygen evolution reaction activity of perovskite oxynitrides. *ACS Materials Letters* **2019**, *1*, 52–57.

(41) Ninova, S.; Aschauer, U. Surface structure and anion order of the oxynitride $LaTiO_2N$. *Journal of Materials Chemistry A* **2017**, *5*, 11040–11046.

(42) Rong, X.; Kolpak, A. M. Ab initio approach for prediction of oxide surface structure, stoichiometry, and electrocatalytic activity in aqueous solution. *The Journal of Physical Chemistry Letters* **2015**, *6*, 1785–1789.

(43) Mulliken, R. S. A new electroaffinity scale; together with data on valence states and on valence ionization potentials and electron affinities. *The Journal of Chemical Physics* **1934**, *2*, 782–793.

(44) Rodionov, I. A.; Zvereva, I. A. Photocatalytic activity of layered perovskite-like oxides in practically valuable chemical reactions. *Russian Chemical Reviews* **2016**, *85*, 248–279.

(45) Zeng, W.; Bian, Y.; Cao, S.; Ma, Y.; Liu, Y.; Zhu, A.; Tan, P.; Pan, J. Phase transformation synthesis of strontium tantalum oxynitride-based heterojunction for improved visible light-driven hydrogen evolution. *ACS Applied Materials & Interfaces 10*, 21328–21334.

(46) Rossmeisl, J.; Qu, Z.-W.; Zhu, H.; Kroes, G.-J.; Nørskov, J. K. Electrolysis of water on oxide surfaces. *Journal of Electroanalytical Chemistry* **2007**, *607*, 83–89.

Graphical TOC Entry